Interferographic TEM Beamforming Resolution

Bryan James[1], Kyubo Noh[2], Andrei Swidinsky[2], Johannes Stoll[3], and Daryl Ball[4]
[1]Electromagnetic Geophysical Imaging Solutions, LLC
[2]University of Toronto, Department of Earth Sciences
[3]Mobile Geophysical Technologies GmbH
[4]Glencore Canada Corporation

SUMMARY

A new method called Interferographic Transient Electromagnetics (ITEM), for semi-airborne multi-source, multi-receiver TEM data, is described using beamforming techniques to synthetically form impulsive distributions of TEM fields that partially unmix TEM signal returns from the subsurface and improve resolution of subsurface geoelectric structure. ITEM differs from application of the wave propagation synthetic aperture concept to diffusive EM geophysics, which achieves no vertical compaction. ITEM achieves full beamforming by using both spatial and temporal sets of subsurface electric field distributions to form a space-time digital filter that yields significant impulsive TEM field compaction in both horizontal and vertical dimensions. The ITEM concept is described for a 2D geometry. ITEM processing is applied to a reference model set of electric field distributions as well as both reference model and acquired magnetic field profiles. The resulting filtered distributions are translated into a subsurface resistivity image using a simple image formation process. An example for a synthetic geoelectric structure is provided that demonstrates ITEM processing and subsurface imaging. A further simulated test of ITEM resolution improvement is based on determining the minimum visible distance between two conductors in comparison to that seen in the original TEM fields. An initial test of ITEM processing on field TEM data is performed on data acquired at Raglan Mine, Quebec.

Keywords: transient electromagnetics, beamforming, semi-airborne, imaging

INTRODUCTION

Many applications of electromagnetic (EM) geophysics could benefit from improvements in localized spatial resolution of geoelectric properties. The achievable resolution is significantly constrained by the diffusing distribution of current density induced in the subsurface which loses curvature increasingly with time (or decreasing frequency) and depth of diffusion. Measured magnetic fields above the earth's surface are coupled to all of the subsurface current density at all locations, with the result that there is considerable overlap in signals from different zones, limiting resolution.

A promising avenue for EM resolution improvements is to sharpen the electric field distribution in the earth created by EM sources, whether by synthetic or physically real means. In a variety of adjacent technical disciplines [such as Radio Frequency signals intelligence (Tuncer and Friedlander, 2009), synthetic aperture radar (Moreira et al, 2013; Jakowatz et al, 2012), radio astronomy (Levanda et al, 2009), and medical imaging (Jensen, et al, 2006; Feng et al, 2001)] a very powerful technique is the weighted combination of multiple sources and/or sensors to create a synthetic aperture (SA). A SA increases the lateral focusing of a signal that is controlled by the overall length of the source or receiver set. A key characteristic of wave propagation SA techniques is that range resolution is very good due to the inherent separation of propagating signals in time. This ingredient is greatly reduced for the EM diffusion geophysics case, and significantly weakens the utility of the SA concept for EM applications. Even so, efforts toward the use of SA concepts have been made in frequency-domain marine controlled source EM (Fan et al, 2010; Knaak et al, 2015; Tu and Zhdanov, 2020). A SA EM method has been described for terrestrial application to mineral exploration problems by Kolaj and Smith (2015).

While the SA concept is powerful for wave propagation problems, it is only a means to the end called beamforming. Beamforming is the concept of synthetically creating the ability to sense a signal coming from, or send a signal going to, a highly localized point in space. SA beamforming for wave propagation is solely a spatial filter, with coefficients adapted for different target locations. The SA concept is incomplete, however, for EM diffusion beamforming precisely because of the substantial loss of time separation of returns from different ranges (depths). For EM diffusion a SA achieves no vertical EM field compaction. Beamforming itself is the more useful concept for sharpening diffusive TEM field structure.

We pursue maximal synthetic concentration of the electromagnetic field for any point in the subsurface as this will provide enhanced spatial resolution of subsurface features. The beamforming approach uses a field

interference approach accomplishing both constructive and destructive interference to concentrate field structure where desired and reduce the field everywhere else. Therefore, the new beamforming algorithm is called Interferographic TEM (ITEM) to reflect this physics basis, as well as to avoid confusion with SA processing. Accomplishing full beamforming for TEM requires a multi-dimensional filter operating both over a number of sources as well as over time. Here the use of the time dimension serves as a proxy for the z-direction, since diffusion steadily penetrates to greater depths as time increases. The use of multiple TEM sources in an integrated manner is not new (James and Borns, 1993; Wright et al., 2002; Oldenburg et al., 2013). Designing filters to combine the subsurface electric fields from multiple sources over time into a compact synthetic subsurface electromagnetic field structure is a new step for TEM applications.

A prime candidate for a terrestrial ITEM geophysics system is the semi-airborne survey design (Elliott, 1998; Smith et al., 2001), consisting of multiple sources on the ground and airborne magnetic field receivers. Much recent activity is occurring in drone-based semi-airborne EM geophysics as it rapidly gains in utility (Ito et al., 2014; Becken et al., 2020; Stoll et al., 2020).

ITEM Beamforming and Resistivity Imaging

We formulate a 2-D problem, assuming data distributed in (x,t), to form a subsurface image in a (x,z) plane, to simplify the concept description. This development uses an array of grounded wire sources distributed in the 'x' direction, that are oriented in the 'y' direction (orthogonal to the profile). Loop sources work as well.

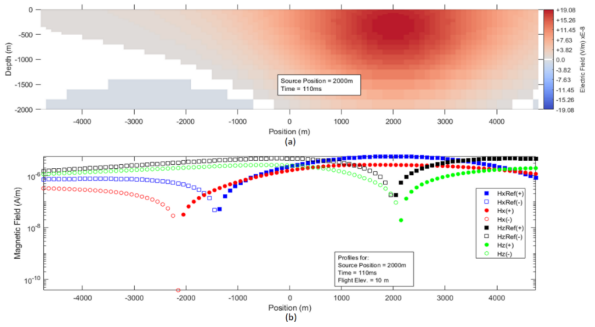

Figure 1: (a) X-Z cross-section of E_y in the earth at time = 110 ms for a grounded wire source oriented in the 'y' direction at position x = 2000 m for a halfspace model of 10 ohm-m. (b) Example H_x and H_z profiles, simulated as collected by a drone flying 10 m above the earth surface, corresponding to E_y in (a). Square symbols denote reference data. Circles denote acquired data. Positive values are filled symbols; negative values are open symbols. Blue denotes reference H_x and black denotes reference H_z. Acquired field data are red for H_x and green for H_z.

The TEM beamforming algorithm uses the electric field (E) distributions (e.g., see Figure 1), for a reference model, for a number of source positions (NX_s) as well as for all of the times (NT) collected ($NX_s \cdot NT = N_{st}$ unique E distributions) to construct, via weighted summation, a virtual E_f distribution ('*f*' for filter) centered on a desired subsurface location. E_f is as localized as possible given the set of individual subsurface E distributions available as inputs. The space-time weights form a digital filter. The physical effect is equivalent to generating an interference pattern from the numerous individual E distributions (weights create both constructive and destructive interference) to build an E_f distribution centered at a desired position that is much more compact than occurs for any original E distribution at that position at one time from one source. The computation of weights is performed for a gridded subsurface (with $NX \cdot NZ = N_{xz}$ locations) where a unique set of (x_s,t) weights occurs for each subsurface position.

The ITEM weight coefficient derivation closely follows that in Fuchs (2007) for medical magnetoencephalogram (MEG) imaging. In TEM geophysics the electric field is everywhere in the subsurface and so ITEM forms smeared impulsive E_f distributions. ITEM weights constitute a beamformer that creates compact E_f distributions centered at all desired subsurface positions in a x-z plane. The weights are then also applied to acquired and reference model magnetic field data to form filtered magnetic field profiles, H_f.

We find a set of coefficients $W(x_s,t;x,z)$, where x_s is source position and t is time, that produces electric field distributions that are maximally compact and centered at subsurface positions denoted by '*x,z*'. The solution for the beamformer weights uses the Lagrange multipliers method. The beamformer coefficients are, in matrix form,

$$\mathbf{W} = \frac{\mathbf{C}^{-1} \cdot \mathbf{E}^{\mathrm{T}}}{\mathbf{E} \cdot \mathbf{C}^{-1} \cdot \mathbf{E}^{\mathrm{T}}} . \qquad (1)$$

W is a N_{st} by N_{xz} matrix, **E** is the set of input E distributions, and **C** is the correlation matrix of all input E distributions. The filtering equations to obtain E_f distributions and H_f profiles are, in matrix form,

$$\mathbf{E}_{\mathrm{f}} = \mathbf{E} \cdot \mathbf{W} \quad , \text{and} \qquad (2)$$

$$\mathbf{H}_{\mathrm{f}} = \mathbf{H} \cdot \mathbf{W} . \qquad (3)$$

Figure 2 is an example of *W* variations for a simple 10 ohm-m halfspace reference model for producing an E_f distribution centered on one cell position. The weighting coefficients display oscillatory behavior which have the equivalent physical effect of constructive and destructive interference. The interference result is shown in Figure 3. Most of the resulting interference pattern across the subsurface grid are small amplitude sidelobes (destructive

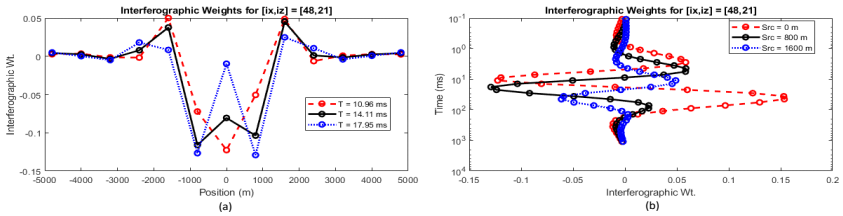

Figure 2: Selected weighting coefficients for the E_f distribution centered on one subsurface position calculated for the halfspace reference model. (a) Weights vs. source positions for 3 adjacent times. (b) Weights vs. time for 3 adjacent sources; early times reflect shallow E distributions and later times reflect deeper E distributions.

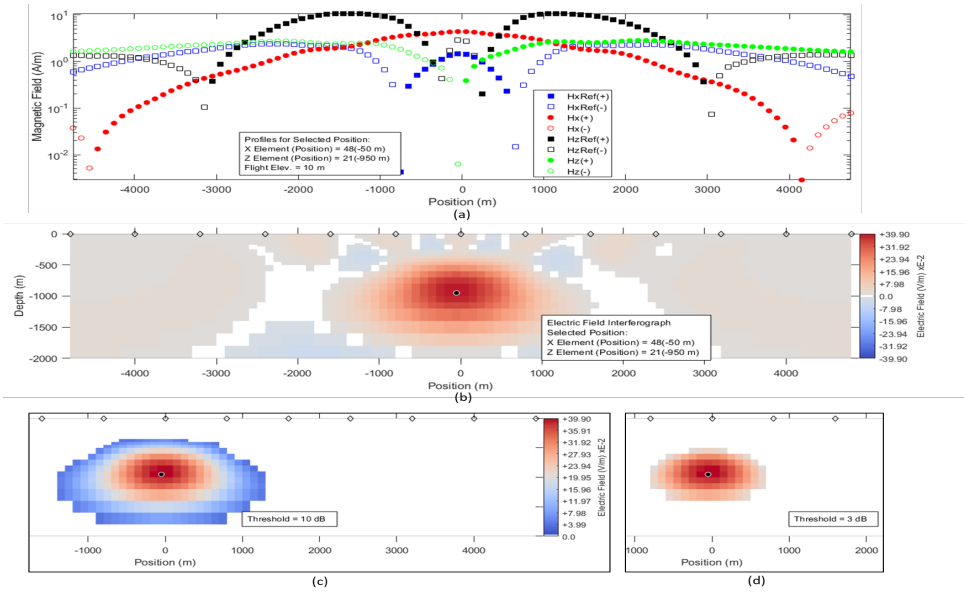

Figure 3: Filtering results for one element in the subsurface. (a) Calculated H_f profiles, simulated as being collected by a drone flying 10 m above the earth surface. Symbols are as described for Figure 1. (b) Calculated E_f distribution. The diamond symbols at the top of the cross-section denote the source positions used for calculation inputs. (c) E_{ft} distribution after 10 dB threshold. (d) E_{ft} distribution after 3 dB threshold. The colorbar displayed in (c) is also used for (d). The E_f and E_{ft} distributions all display a black dot at the designated cell position.

interference), leaving one main lobe that is as small as the inputs allow (constructive interference).

The raw E_f distributions (e.g., Figure 3(b)) should be reduced to some part of their main lobe for purposes of synthesizing a resistivity image. Figure 3 shows E_{ft} ('t' for threshold) for both 10 dB and 3 dB (½ of peak amplitude) thresholds. 3 dB follows signal processing norms and is the ITEM default.

The difference between acquired and reference H_f data, for a specific (x,z) subsurface position, is used in an image formation process (IFP) where it is related back to the E_{ft} distribution centered at (x,z). An increase in acquired H_f relative to reference H_f indicates greater current density J, and vice versa; greater J translates into higher conductivity, and vice versa, for the elements in that compact distribution – a linear relationship is assumed. The linear assumption is good for small resistivity contrasts but increases in error for larger changes. This IFP exclusively uses the H_x data at present; the H_{xf} profiles are maximum and almost symmetric above the E_{ft} distribution in Figure 3(a). In contrast, the H_{zf} profiles are more complicated. The algorithm is as follows.

Each filtered output, for each and every (x_i,z_i) position, is a distribution in the (x_k,z_k) domain. 1) Compute the $H_{xf}(x_k)$ profile residual for each (x_i,z_i). 2) Sum over all of the $E_{ft}(x_i,z_i)$ distributions for each (x_k,z_k). 3) Repeat the summation but with the $H_{xf}(x_k)$ profile residual multiplied with the associated $E_{ft}(x_k,z_k)$ values (i.e., point-by-point in x_k) for each (x_i,z_i). 4) Ratio the residual H mediated summation by the simple E summation, which is an estimate of the change in current density, Δj, in each cell. This ratio maps into a resistivity estimate, ρ_{est}, for each (x_k,z_k) cell as

$$\rho_{est}(x_k, z_k) = \rho_{ref}(x_k, z_k)/(1 + \Delta j(x_k, z_k)). \quad (4)$$

Issues arise with (4) for $\Delta j <= -1$; as Δj approaches -1 the $1 + \Delta j$ term is changed to $10^{\Delta j}$, which is nonlinear.

Results

A simulated test for semi-airborne survey design is utilized with 13 grounded wire sources, each 1000 m long, oriented in the y-direction (perpendicular to x-direction profile) that are separated by 800 m, for a total profile length of 9600 m. A subsurface grid of dimensions 9600 m in x and 2000 m in z is used for the subsurface E distributions. H measurements for each source are simulated for a drone 10 m above the earth's surface. The simulated model is the buried basin shown in Figure 4. The acquired data displayed in Figure 3 are for this simulated buried basin. The resistivity image resulting from ITEM processing is shown in Figure 5. This image result uses a gradational layered reference model of increasing resistivity with depth. This first result can be used to generate a new reference model, and the ITEM process repeated, in an iterative cycle until convergence is achieved between the acquired and reference H_{xf} data. First ITEM processing of TEM field data, from Raglan Mine in northern Quebec, is shown in Figure 6.

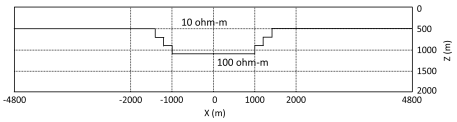

Figure 4: Buried basin model used to simulate acquired magnetic field profile data for ITEM processing.

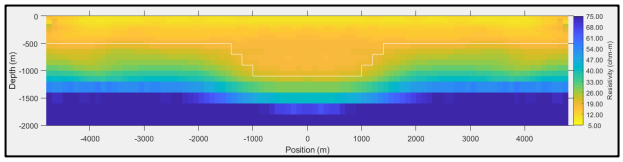

Figure 5: Resistivity image for ITEM processing of simulated buried basin data. The basin model is superimposed.

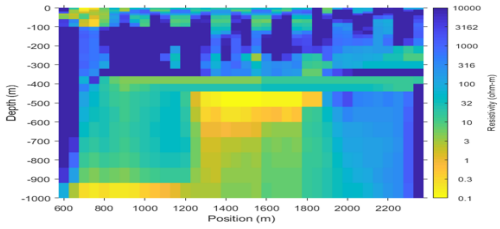

Figure 6: Resistivity image from ITEM processing of TEM field data at Raglan Mine, Quebec.

Finally, a resolution exercise in which the minimum visible distance between two conductors is found is conducted to highlight the reduction in minimum distance achieved with ITEM processing vs. the original TEM magnetic profile data. The ITEM results show a reduction of about 40% in the minimum visible separation in this comparison.

Discussion

ITEM beamforming is a method to synthetically sharpen the shape of the TEM field. In effect, it partially *unmixes* the signal returns from different parts of the medium. This enables improved resolution relative to the resolution achievable with the original TEM field structure in which the signal returns are highly *mixed*. The signal mixing/unmixing concept being used here is completely analogous to the wave propagation case for synthetic aperture radar (SAR). In SAR a single RF beam actually has broad coverage of a ground scene, with all of the signal returns from different scene elements mixed together. The use of many such broad RF beams from different positions covering the same ground scene enables the SA processing method to unmix all of the signal returns from the many scene elements and produce an image with very high spatial resolution that is mostly set by the RF signal frequency (and equivalent wavelength) as well as the length of the SA. For TEM the signal returns come from earth elements distributed both laterally and vertically. The degree of signal return unmixing from ITEM processing is set by the location of the TEM sources as well as the spatial variation of the diffusing TEM field, which is much broader than the SAR case. This limit to signal return unmixing sets the degree of geoelectric structural resolution attainable.

Conclusion

A new method of TEM data synthesis called Interferographic TEM is introduced. ITEM implements a full beamforming solution as a space-time digital filter to increase localization of EM field structure in filtering results for both subsurface E distributions and H profiles. The new method uses distributions in both space and time to achieve field compaction in both lateral and vertical dimensions. These interferographic products are used to produce a resistivity image section. An example for a simulated structure shows a good resistivity image facsimile of the structure is obtained by ITEM processing. A first field example with ITEM processing is also shown for TEM data at Raglan Mine, Quebec. The process may be generalized into an iterative cycle to improve results until model convergence is reached. Also, a two-conductor resolution test shows ITEM reduces the minimum separation at which the two are visibly distinguishable in comparison to the original TEM profiles by about 40%.

REFERENCES

Becken, M., Nittinger, C., Smirnova, M., Steuer, A., Martin, T., Petersen, H., Meyer, U., Mörbe, W., Yogeshwar, P., Tezkan, B., Matzander, U., Friedrichs, B., Rochlitz, R., Günther, T., Schiffler, M., and Stolz, R., and the DESMEX Working Group, 2020, DESMEX: A novel system development for semi-airborne electromagnetic exploration: GEOPHYSICS, **85**, no. 6, E253-E267.

Elliott, P., 1998, The Principles and practice of FLAIRTEM: Exploration Geophysics, **29** (1/2), 58-60.

Fan, Y., Snieder, R., Slob, E., Hunziker, J., Singer, J., Sheiman, J., and Rosenquist, M., 2010, Synthetic aperture controlled source electromagnetics: Geophys. Res. Lett., **37**, no. 13, L13305.

Feng, D., Xu, Y., Ku, G., and Wang, L., 2001, Microwave-induced thermoacoustic tomography: Reconstruction by synthetic aperture: Medical Physics, **28**, no. 12, 2427-2431.

Fuchs, A., Beamforming and Its Applications to Brain Connectivity, 2007, In *Handbook of Brain Connectivity. Understanding Complex Systems.* Springer, Berlin, Heidelberg, pp. 357-378.

Ito, H., Kaieda, H., Mogi, T., and Jomori, A., 2014, Grounded electrical-source airborne transient electromagnetics (GREATEM) survey of Aso Volcano, Japan: Exploration Geophysics, **45**, no.1.

Jakowatz, C., Wahl, D., Eichel, P., Ghiglia, D., and Thompson, P., Spotlight-Mode Synthetic Aperture Radar: A Signal Processing Approach, 2012, Springer Science+Business Media.

James, B., and Borns, D., 1993, Transient electromagnetic two-dimensional subsurface resistivity imaging near the Waste Isolation Pilot Plant, Carlsbad, New Mexico: SAND report, Sandia National Laboratories, Albuquerque, New Mexico.

Jensen, J., Gammelmark, K., and Pedersen, M., 2006, Synthetic aperture ultrasound imaging: Ultrasonics, **44**, pp. e5-e15.
Knaak, A., Snieder, R., Suilleabhain, L., Fan, Y., and Ramirez-Mejia, D., 2015, Optimized 3D synthetic aperture for controlled-source electromagnetics: GEOPHYSICS, **80**, no. 6, E309-E316.

Kolaj, M., and Smith, R., 2015, A multiple transmitter and receiver electromagnetic system for improved target detection: GEOPHYSICS, **80**, no. 4, E247-E255.

Levanda, R., and Leshem, A., 2009, Synthetic aperture radio telescopes: IEEE Signal Processing Magazine, **27**, no. 1, 14-29.

Moreira, A., Prats-Iraola, P., Younis, M., Krieger, G., Hajnsek, I., and Papathanassiou, K., 2013, A tutorial on synthetic aperture radar: IEEE Geoscience and Remote Sensing Magazine, **1**, no. 1, 6-43.

Oldenburg, D., Haber, E., and Shekhtman, R., 2013, Three dimensional inversion of multisource time domain electromagnetic data: GEOPHYSICS, **78**, no. 1, E47-E57.

Smith, R., Annan, A., and McGowan, P., 2001, A comparison of data from airborne, semi-airborne, and ground electromagnetic systems: GEOPHYSICS, **66**, no. 5, 1379–1385.

Stoll, J., Noellenburg, R., Kordes, T., 2020, Semi-Airborne electromagnetics using a multicopter: Fast Times, **25**, no. 3, 106-113.

Tu, X., and Zhdanov, M., 2020, Robust synthetic aperture imaging of marine controlled-source electromagnetic data: IEEE Transactions on Geoscience and Remote Sensing, **58**, no. 8, 5527-5539.

Tuncer, E., and Friedlander, B., (Eds.), 2009, Classical and modern direction-of-arrival estimation: Academic Press.

Wright, D., Ziolkowski, A., and Hobbs, B., 2002, Hydrocarbon detection and monitoring with a multichannel transient electromagnetic (MTEM) survey: The Leading Edge, vol. 21, 852-864